$K(892)^*$ resonance production in Au+Au and $p + p$ collisions at $\sqrt{s_{NN}} = 200$ GeV

J. Adams,[3] M. M. Aggarwal,[29] Z. Ahammed,[43] J. Amonett,[20] B. D. Anderson,[20] D. Arkhipkin,[13] G. S. Averichev,[12] S. K. Badyal,[19] Y. Bai,[27] J. Balewski,[17] O. Barannikova,[32] L. S. Barnby,[3] J. Baudot,[18] S. Bekele,[28] V. V. Belaga,[12] R. Bellwied,[46] J. Berger,[14] B. I. Bezverkhny,[48] S. Bharadwaj,[33] A. Bhasin,[19] A. K. Bhati,[29] V. S. Bhatia,[29] H. Bichsel,[45] A. Billmeier,[46] L. C. Bland,[4] C. O. Blyth,[3] B. E. Bonner,[34] M. Botje,[27] A. Boucham,[38] A. V. Brandin,[25] A. Bravar,[4] M. Bystersky,[11] R. V. Cadman,[1] X. Z. Cai,[37] H. Caines,[48] M. Calderón de la Barca Sánchez,[17] J. Castillo,[21] D. Cebra,[7] Z. Chajecki,[44] P. Chaloupka,[11] S. Chattopadhyay,[43] H. F. Chen,[36] Y. Chen,[8] J. Cheng,[41] M. Cherney,[10] A. Chikanian,[48] W. Christie,[4] J. P. Coffin,[18] T. M. Cormier,[46] J. G. Cramer,[45] H. J. Crawford,[6] D. Das,[43] S. Das,[43] M. M. de Moura,[35] A. A. Derevschikov,[31] L. Didenko,[4] T. Dietel,[14] S. M. Dogra,[19] W. J. Dong,[8] X. Dong,[36] J. E. Draper,[7] F. Du,[48] A. K. Dubey,[15] V. B. Dunin,[12] J. C. Dunlop,[4] M. R. Dutta Mazumdar,[43] V. Eckardt,[23] W. R. Edwards,[21] L. G. Efimov,[12] V. Emelianov,[25] J. Engelage,[6] G. Eppley,[34] B. Erazmus,[38] M. Estienne,[38] P. Fachini,[4] J. Faivre,[18] R. Fatemi,[17] J. Fedorisin,[12] K. Filimonov,[21] P. Filip,[11] E. Finch,[48] V. Fine,[4] Y. Fisyak,[4] K. Fomenko,[12] J. Fu,[41] C. A. Gagliardi,[39] L. Gaillard,[3] J. Gans,[48] M. S. Ganti,[43] L. Gaudichet,[38] F. Geurts,[34] V. Ghazikhanian,[8] P. Ghosh,[43] J. E. Gonzalez,[8] O. Grachov,[46] O. Grebenyuk,[27] D. Grosnick,[42] S. M. Guertin,[8] Y. Guo,[46] A. Gupta,[19] T. D. Gutierrez,[7] T. J. Hallman,[4] A. Hamed,[46] D. Hardtke,[21] J. W. Harris,[48] M. Heinz,[2] T. W. Henry,[39] S. Hepplemann,[30] B. Hippolyte,[18] A. Hirsch,[32] E. Hjort,[21] G. W. Hoffmann,[40] H. Z. Huang,[8] S. L. Huang,[36] E. W. Hughes,[5] T. J. Humanic,[28] G. Igo,[8] A. Ishihara,[40] P. Jacobs,[21] W. W. Jacobs,[17] M. Janik,[44] H. Jiang,[8] P. G. Jones,[3] E. G. Judd,[6] S. Kabana,[2] K. Kang,[41] M. Kaplan,[9] D. Keane,[20] V. Yu. Khodyrev,[31] J. Kiryluk,[22] A. Kisiel,[44] E. M. Kislov,[12] J. Klay,[21] S. R. Klein,[21] D. D. Koetke,[42] T. Kollegger,[14] M. Kopytine,[20] L. Kotchenda,[25] M. Kramer,[26] P. Kravtsov,[25] V. I. Kravtsov,[31] K. Krueger,[1] C. Kuhn,[18] A. I. Kulikov,[12] A. Kumar,[29] R. Kh. Kutuev,[13] A. A. Kuznetsov,[12] M. A. C. Lamont,[48] J. M. Landgraf,[4] S. Lange,[14] F. Laue,[4] J. Lauret,[4] A. Lebedev,[4] R. Lednicky,[12] S. Lehocka,[12] M. J. LeVine,[4] C. Li,[36] Q. Li,[46] Y. Li,[41] G. Lin,[48] S. J. Lindenbaum,[26] M. A. Lisa,[28] F. Liu,[47] L. Liu,[47] Q. J. Liu,[45] Z. Liu,[47] T. Ljubicic,[4] W. J. Llope,[34] H. Long,[8] R. S. Longacre,[4] M. Lopez-Noriega,[28] W. A. Love,[4] Y. Lu,[47] T. Ludlam,[4] D. Lynn,[4] G. L. Ma,[37] J. G. Ma,[8] Y. G. Ma,[37] D. Magestro,[28] S. Mahajan,[19] D. P. Mahapatra,[15] R. Majka,[48] L. K. Mangotra,[19] R. Manweiler,[42] S. Margetis,[20] C. Markert,[20] L. Martin,[38] J. N. Marx,[21] H. S. Matis,[21] Yu. A. Matulenko,[31] C. J. McClain,[1] T. S. McShane,[10] F. Meissner,[21] Yu. Melnick,[31] A. Meschanin,[31] M. L. Miller,[22] N. G. Minaev,[31] C. Mironov,[20] A. Mischke,[27] D. K. Mishra,[15] J. Mitchell,[34] B. Mohanty,[43] L. Molnar,[32] C. F. Moore,[40] D. A. Morozov,[31] M. G. Munhoz,[35] B. K. Nandi,[43] S. K. Nayak,[19] T. K. Nayak,[43] J. M. Nelson,[3] P. K. Netrakanti,[43] V. A. Nikitin,[13] L. V. Nogach,[31] S. B. Nurushev,[31] G. Odyniec,[21] A. Ogawa,[4] V. Okorokov,[25] M. Oldenburg,[21] D. Olson,[21] S. K. Pal,[43] Y. Panebratsev,[12] S. Y. Panitkin,[4] A. I. Pavlinov,[46] T. Pawlak,[44] T. Peitzmann,[27] V. Perevoztchikov,[4] C. Perkins,[6] W. Peryt,[44] V. A. Petrov,[13] S. C. Phatak,[15] R. Picha,[7] M. Planinic,[49] J. Pluta,[44] N. Porile,[32] J. Porter,[45] A. M. Poskanzer,[21] M. Potekhin,[4] E. Potrebenikova,[12] B. V. K. S. Potukuchi,[19] D. Prindle,[45] C. Pruneau,[46] J. Putschke,[23] G. Rakness,[30] R. Raniwala,[33] S. Raniwala,[33] O. Ravel,[38] R. L. Ray,[40] S. V. Razin,[12] D. Reichhold,[32] J. G. Reid,[45] G. Renault,[38] F. Retiere,[21] A. Ridiger,[25] H. G. Ritter,[21] J. B. Roberts,[34] O. V. Rogachevskiy,[12] J. L. Romero,[7] A. Rose,[46] C. Roy,[38] L. Ruan,[36] R. Sahoo,[15] I. Sakrejda,[21] S. Salur,[48] J. Sandweiss,[48] M. Sarsour,[17] I. Savin,[13] P. S. Sazhin,[12] J. Schambach,[40] R. P. Scharenberg,[32] N. Schmitz,[23] K. Schweda,[21] J. Seger,[10] P. Seyboth,[23] E. Shahaliev,[12] M. Shao,[36] W. Shao,[5] M. Sharma,[29] W. Q. Shen,[37] K. E. Shestermanov,[31] S. S. Shimanskiy,[12] E. Sichtermann,[21] F. Simon,[23] R. N. Singaraju,[43] G. Skoro,[12] N. Smirnov,[48] R. Snellings,[27] G. Sood,[42] P. Sorensen,[21] J. Sowinski,[17] J. Speltz,[18] H. M. Spinka,[1] B. Srivastava,[32] A. Stadnik,[12] T. D. S. Stanislaus,[42] R. Stock,[14] A. Stolpovsky,[46] M. Strikhanov,[25] B. Stringfellow,[32] A. A. P. Suaide,[35] E. Sugarbaker,[28] C. Suire,[4] M. Sumbera,[11] B. Surrow,[22] T. J. M. Symons,[21] A. Szanto de Toledo,[35] P. Szarwas,[44] A. Tai,[8] J. Takahashi,[35] A. H. Tang,[27] T. Tarnowsky,[32] D. Thein,[8] J. H. Thomas,[21] S. Timoshenko,[25] M. Tokarev,[12] T. A. Trainor,[45] S. Trentalange,[8] R. E. Tribble,[39] O. D. Tsai,[8] J. Ulery,[32] T. Ullrich,[4] D. G. Underwood,[1] A. Urkinbaev,[12] G. Van Buren,[4] M. van Leeuwen,[21] A. M. Vander Molen,[24] R. Varma,[16] I. M. Vasilevski,[13] A. N. Vasiliev,[31] R. Vernet,[18] S. E. Vigdor,[17] Y. P. Viyogi,[43] S. Vokal,[12] S. A. Voloshin,[46] M. Vznuzdaev,[25] W. T. Waggoner,[10] F. Wang,[32] G. Wang,[20] G. Wang,[5] X. L. Wang,[36] Y. Wang,[40] Y. Wang,[41] Z. M. Wang,[36] H. Ward,[40] J. W. Watson,[20] J. C. Webb,[17] R. Wells,[28] G. D. Westfall,[24] A. Wetzler,[21] C. Whitten Jr.,[8] H. Wieman,[21] S. W. Wissink,[17] R. Witt,[2] J. Wood,[8] J. Wu,[36] N. Xu,[21] Z. Xu,[4] Z. Z. Xu,[36] E. Yamamoto,[21] P. Yepes,[34] V. I. Yurevich,[12] Y. V. Zanevsky,[12] H. Zhang,[4] W. M. Zhang,[20] Z. P. Zhang,[36] R. Zoulkarneev,[13] Y. Zoulkarneeva,[13] and A. N. Zubarev[12]

(STAR Collaboration)

[1]*Argonne National Laboratory, Argonne, Illinois 60439, USA*

[2]*University of Bern, CH-3012 Bern, Switzerland*

[3]*University of Birmingham, Birmingham, United Kingdom*

[4]*Brookhaven National Laboratory, Upton, New York 11973, USA*

[5]*California Institute of Technology, Pasadena, California 91125, USA*

[6]*University of California, Berkeley, California 94720, USA*

[7]*University of California, Davis, California 95616, USA*

[8]*University of California, Los Angeles, California 90095, USA*

[9]*Carnegie Mellon University, Pittsburgh, Pennsylvania 15213, USA*

[10]*Creighton University, Omaha, Nebraska 68178, USA*

[11]*Nuclear Physics Institute AS CR, 250 68 Rez/Prague, Czech Republic*
[12]*Laboratory for High Energy (JINR), Dubna, Russia*
[13]*Particle Physics Laboratory (JINR), Dubna, Russia*
[14]*University of Frankfurt, Frankfurt, Germany*
[15]*Institute of Physics, Bhubaneswar 751005, India*
[16]*Indian Institute of Technology, Mumbai, India*
[17]*Indiana University, Bloomington, Indiana 47408, USA*
[18]*Institut de Recherches Subatomiques, Strasbourg, France*
[19]*University of Jammu, Jammu 180001, India*
[20]*Kent State University, Kent, Ohio 44242, USA*
[21]*Lawrence Berkeley National Laboratory, Berkeley, California 94720, USA*
[22]*Massachusetts Institute of Technology, Cambridge, Massachusetts 02139-4307, USA*
[23]*Max-Planck-Institut für Physik, Munich, Germany*
[24]*Michigan State University, East Lansing, Michigan 48824, USA*
[25]*Moscow Engineering Physics Institute, Moscow, Russia*
[26]*City College of New York, New York, New York 10031, USA*
[27]*NIKHEF, Amsterdam, The Netherlands*
[28]*Ohio State University, Columbus, Ohio 43210, USA*
[29]*Panjab University, Chandigarh 160014, India*
[30]*Pennsylvania State University, University Park, Pennsylvania 16802, USA*
[31]*Institute of High Energy Physics, Protvino, Russia*
[32]*Purdue University, West Lafayette, Indiana 47907, USA*
[33]*University of Rajasthan, Jaipur 302004, India*
[34]*Rice University, Houston, Texas 77251, USA*
[35]*Universidade de São Paulo, São Paulo, Brazil*
[36]*University of Science & Technology of China, Anhui 230027, China*
[37]*Shanghai Institute of Applied Physics, Shanghai 201800, China*
[38]*SUBATECH, Nantes, France*
[39]*Texas A&M University, College Station, Texas 77843, USA*
[40]*University of Texas, Austin, Texas 78712, USA*
[41]*Tsinghua University, Beijing 100084, China*
[42]*Valparaiso University, Valparaiso, Indiana 46383, USA*
[43]*Variable Energy Cyclotron Centre, Kolkata 700064, India*
[44]*Warsaw University of Technology, Warsaw, Poland*
[45]*University of Washington, Seattle, Washington 98195, USA*
[46]*Wayne State University, Detroit, Michigan 48201, USA*
[47]*Institute of Particle Physics, CCNU (HZNU), Wuhan 430079, China*
[48]*Yale University, New Haven, Connecticut 06520, USA*
[49]*University of Zagreb, Zagreb, HR-10002, Croatia*
(Received 9 December 2004; published 6 June 2005)

The short-lived $K(892)^*$ resonance provides an efficient tool to probe properties of the hot and dense medium produced in relativistic heavy-ion collisions. We report measurements of K^* in $\sqrt{s_{NN}} = 200$ GeV Au+Au and $p + p$ collisions reconstructed via its hadronic decay channels $K(892)^{*0} \to K\pi$ and $K(892)^{*\pm} \to K^0_S\pi^\pm$ using the STAR detector at the Relativistic Heavy Ion Collider at Brookhaven National Laboratory. The K^{*0} mass has been studied as a function of p_T in minimum bias $p + p$ and central Au+Au collisions. The K^* p_T spectra for minimum bias $p + p$ interactions and for Au+Au collisions in different centralities are presented. The K^*/K yield ratios for all centralities in Au+Au collisions are found to be significantly lower than the ratio in minimum bias $p + p$ collisions, indicating the importance of hadronic interactions between chemical and kinetic freeze-outs. A significant nonzero K^{*0} elliptic flow (v_2) is observed in Au+Au collisions and is compared to the K^0_S and Λ v_2. The nuclear modification factor of K^* at intermediate p_T is similar to that of K^0_S but different from Λ. This establishes a baryon-meson effect over a mass effect in the particle production at intermediate p_T ($2 < p_T \leqslant 4$ GeV/c).

DOI: 10.1103/PhysRevC.71.064902 PACS number(s): 25.75.Dw, 13.75.Cs

I. INTRODUCTION

Lattice QCD calculations [1] predict a phase transition from hadronic matter to quark gluon plasma (QGP) at high temperatures and/or high densities. Matter under such extreme conditions can be studied in the laboratory by colliding heavy nuclei at very high energies. The Relativistic Heavy Ion Collider (RHIC) at Brookhaven National Laboratory provides collisions of heavy nuclei and protons at center of mass energies up to $\sqrt{s_{NN}} = 200$ GeV. The initial stage of these collisions can be described as the interpenetration of the nuclei with partonic interactions at high energy. With the interactions of the partons in the system, chemical and local thermal equilibrium of the system may be reached and the QGP may form. As the system expands and cools, it will hadronize and chemically freeze out. After a period of hadronic interactions, the system reaches the kinetic freeze-out stage when all hadrons stop interacting [2–4]. After the kinetic freeze-out, particles free-stream toward the detectors where our measurements are performed.

The typical lifetime of a resonance is a few fm/c, which is comparable to the expected lifetime of the hot and dense matter produced in heavy-ion collisions [5]. In a hot and dense system, resonances are in close proximity with other strongly interacting hadrons. The in-medium effect related to the high density and/or high temperature of the medium can modify various resonance properties, such as masses, widths, and even the mass line shapes [6–8]. Thus, measurements of various resonance properties can provide detailed information about the interaction dynamics in relativistic heavy-ion collisions [9,10]. Recent measurements [11] by the FOCUS Collaboration for the K^{*0} from charm decays show that the K^{*0} mass line shape could be changed by the effects of interference from an s wave and possible other sources. Distortions of the line shape of ρ^0 have also been observed at RHIC in $p + p$ and peripheral Au+Au collisions [12]. Dynamical interactions with the surrounding matter [7,8,13], interference between various scattering channels [14], phase-space distortions [7,8,13,15–20], and Bose-Einstein correlations [7,8,15,18–20] are possible explanations for the apparent modification of resonance properties.

Resonance measurements in the presence of a dense medium can be significantly affected by two competing effects. Resonances that decay before kinetic freeze-out may not be reconstructed owing to the rescattering of the daughter particles. In this case, the lost efficiency in the reconstruction of the parent resonance is relevant and depends on the time between chemical and kinetic freeze-outs, the source size, the resonance phase-space distribution, the resonance daughters' hadronic interaction cross sections, etc. However, after chemical freeze-out, pseudoelastic interactions [21] among hadrons in the medium may increase the resonance population. This resonance regeneration depends on the cross section of the interacting hadrons in the medium. Thus, the study of resonances can provide an important probe of the time evolution of the source from chemical to kinetic freeze-outs and detailed information on hadronic interactions in the final stage.

In this paper, we study the $K(892)^*$ vector meson with a lifetime of 4 fm/c. The kaon and pion daughters of the K^* resonance in the hadronic decay channel $K^* \to K\pi$ can interact with other hadrons in the medium. Their rescattering effect is mainly determined by the pion-pion interaction total cross section [22], which was measured to be significantly larger (factor $\sim$5) than the kaon-pion interaction total cross section [23]. The kaon-pion interaction total cross section determines the regeneration effect that produces the K^* resonance [24]. Thus, the final observable K^* yields may decrease compared to the primordial yields, and a suppression of the K^*/K yield ratio is expected in heavy-ion collisions. This K^* yield decrease and the K^*/K suppression compared to elementary collisions, such as $p + p$, at similar collision energies can be used to roughly estimate the system time span between chemical and kinetic freeze-outs. Because of the rescattering of the daughter particles, the low p_T K^* resonances are less likely to escape the hadronic medium before decaying, compared to high p_T K^* resonances. This could alter the K^* transverse mass (m_T) spectra compared to those of other particles with similar masses.

The in-medium effects on the resonance production can be manifested in other observables as well. In a quark coalescence scenario, the elliptic flow (v_2), for noncentral Au+Au collisions, of the K^* resonances produced at chemical freeze-out might be similar to that of kaons [25]. However, at low p_T, the K^* v_2 may be modified by the rescattering effect discussed previously. This rescattering effect also depends on the hadron distributions in the coordinate space in the system at the final stage. Thus, a measurement of the K^* v_2 at p_T 2 GeV/c compared to the kaon v_2 may provide information on the shape of the fireball in the coordinate space at late stages.

A study of the relation of the particle production to its intrinsic properties may reveal its production mechanism. The nuclear modification factor and v_2 have been observed to be different between π, K and p, Λ [26,27]. In a hydrodynamic limit, the transverse momentum spectra of produced particles are determined only by the velocity field and therefore the mass of the produced particle. In a quark coalescence model, particle production is related to its quark content. Since stable mesons (π, K) are usually lighter than stable baryons (p, Λ), the particle type is coupled with the mass. Detailed studies of K^* (and/or ϕ) can be of special importance, as its mass is close to the mass of baryons (p, Λ) but it is a vector meson. In the intermediate p_T range $2 < p_T$ 6 GeV/c, identified hadron v_2 measurements have shown that the hadron v_2 follows a simple scaling of the number of constituent quarks in the hadrons: $v_2(p_T) = n v_2^q(p_T/n)$, where n is the number of constituent quarks of the hadron and v_2^q is the common elliptic flow for single quarks [27]. Therefore, the v_2 for the K^* produced at hadronization should follow the scaling law with $n = 2$. However, for the K^* regenerated through $K\pi \to K^*$ in the hadronic stage, v_2 should follow the scaling law with $n = 4$ [28]. The measured K^* v_2 in the intermediate p_T region may provide information on the K^* production mechanism in the hadronic phase and reveal the particle production dynamics in general. It is inconclusive whether the difference in the nuclear modification factor between K and Λ is due to a baryon-meson effect or simply a mass effect [27]. We can use the unique properties of the K^* to distinguish whether the nuclear modification factor R_{AA} or R_{CP} (defined in Sec. V F.

and in [29] and [27], respectively) in the intermediate p_T region depends on mass or particle species (i.e., meson/baryon). Specifically, we can compare the R_{CP} of K, K^*, and Λ, which contain one strange valence quark and are in groups of (K, K^*) and Λ as mesons versus baryon, or in groups of K and (K^*, Λ) as different masses.

II. EXPERIMENT

The data used in this analysis were taken in the second RHIC run (2001–2002) using the Solenoidal Tracker at RHIC (STAR) with Au+Au and $p + p$ collisions at $\sqrt{s_{NN}} =$ 200 GeV. The primary tracking device of the STAR detector is the time projection chamber (TPC), which is a 4.2-m-long cylinder covering a pseudorapidity range $|\eta| < 1.8$ for tracking with complete azimuthal coverage ($\Delta\phi = 2\pi$) [30].

In Au+Au collisions, a minimum bias trigger was defined by requiring coincidences between two zero-degree calorimeters, which are located in the beam directions at $\theta < 2$ mrad and measure the spectator neutrons. A central trigger corresponding to the top 10% of the inelastic hadronic Au+Au cross section was defined using both the zero-degree calorimeters and the scintillating central trigger barrel, which surrounds the outer cylinder of the TPC and triggers on charged particles in the midpseudorapidity ($|\eta| < 0.5$) region. In $p + p$ collisions, the minimum bias trigger was defined using coincidences between two beam-beam counters that measure the charged particle multiplicity in forward pseudorapidities ($3.3 < |\eta| < 5.0$).

Only events with the primary vertex within ± 50 cm from the center of the TPC along the beam line were selected to ensure uniform acceptance in the η range studied. As a result, about 2×10^6 top 10% central Au+Au, 2×10^6 minimum bias Au+Au, and 6×10^6 minimum bias $p + p$ collision events were used in this analysis. To study the centrality dependence of the K^* production, the events from minimum bias Au+Au collisions were divided into four centrality bins from the most central to the most peripheral collisions: 0–10%, 10–30%, 30–50% and 50–80%, according to the fraction of the charged hadron reference multiplicity (defined in [31]) distribution in all events.

In addition to momentum information, the TPC provides particle identification for charged particles by measuring their ionization energy loss (dE/dx). The TPC measurement of dE/dx as a function of the momentum (p) is shown in Fig. 1. Different bands seen in Fig. 1 represent Bethe-Bloch distributions [32] folded with the experimental resolutions and correspond to different particle species. Charged pions and kaons can be identified with their momenta up to about 0.75 GeV/c whereas protons and antiprotons can be identified with momenta up to about 1.1 GeV/c. To quantitatively describe the particle identification, the variable $N_{\sigma\pi}$ (e.g., pions) was defined as

$$N_{\sigma\pi} = \frac{1}{R} \log \frac{dE/dx_{\text{measured}}}{\langle dE/dx \rangle_{\pi}}, \tag{1}$$

where dE/dx_{measured} is the measured energy loss for a track, $\langle dE/dx \rangle_{\pi}$ is the expected mean energy loss for charged pions

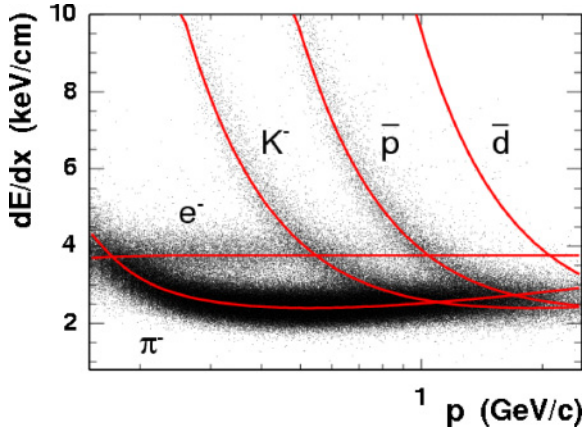

FIG. 1. (Color online) dE/dx for negative particles vs. momentum measured by the TPC in Au+Au collisions. The curves are the Bethe-Bloch parametrization [32] for different particle species.

with a given momentum, and R is the dE/dx resolution, which varies between 6% and 10% from $p + p$ to central Au+Au events and depends on the characteristics of each track, such as the number of dE/dx hits for a track measured in the TPC, the pseudorapidity of a track, etc. We construct $N_{\sigma K}$ in a similar way for the charged kaon identification. Specific analysis cuts (described later) were then applied on $N_{\sigma\pi}$ and $N_{\sigma K}$ to quantitatively select the charged pion and kaon candidate tracks.

III. PARTICLE SELECTIONS

In this analysis, the hadronic decay channels of $K(892)^{*0} \to K^+\pi^-$, $\overline{K(892)^{*0}} \to K^-\pi^+$, and $K(892)^{*\pm} \to K^0_S\pi^\pm$ were measured. In the following, the term K^{*0} stands for K^{*0} or $\overline{K^{*0}}$, and the term K^* stands for K^{*0}, $\overline{K^{*0}}$, or $K^{*\pm}$, unless otherwise specified.

Since the K^* decays in such a short time that the daughters seem to originate from the interaction point, only charged kaon and charged pion candidates whose distance of closest approach to the primary interaction vertex was less than 3 cm were selected. Such candidate tracks are defined as "primary tracks." The charged K^* first undergoes a strong decay to produce a K^0_S and a charged pion herein labeled as the $K^{*\pm}$ daughter pion. Then, the produced K^0_S decays weakly into $\pi^+\pi^-$ with $c\tau = 2.67$ cm. Two oppositely charged pions from the K^0_S decay are called the $K^{*\pm}$ granddaughter pions. The charged daughter pion candidates were selected from primary track samples and the K^0_S candidates were selected through their decay topology.

In Au+Au collisions, charged kaon candidates were selected by requiring $|N_{\sigma K}| < 2$ whereas a looser cut $|N_{\sigma\pi}| < 3$ was applied to select the charged pion candidates to maximize the statistics for the K^{*0} analysis. Such N_σ cuts can only ambiguously select the kaons and pions if applied to the tracks with their momenta beyond the momentum range specified earlier. However, these cuts help to significantly reduce the background. To avoid the acceptance drop in the high-η range, all kaon and pion candidates were required to

have $|\eta| < 0.8$. Kaon and pion candidates were also required to have at least 15 fit points (number of measured TPC hits used in track fit, from a maximum of 45 fit points) to assure track fitting quality and good dE/dx resolution. For all the track candidates, the ratio between the number of TPC track fit points over the maximum possible points was required to be greater than 0.55 to avoid selecting split tracks. To maintain reasonable momentum resolution, only tracks with p_T larger than 0.2 GeV/c were selected.

In $p + p$ collisions, enough data were available to precisely measure the K^{*0} mass, width, and invariant yield as a function of p_T. As statistics was not an issue for this analysis, only kaon candidates with $p < 0.7$ GeV/c were used to ensure clean identification. This kaon momentum cut helped minimize contamination from misidentified correlated pairs and thus reduce the systematic uncertainty. In the case of the pion candidates, the same p and p_T cuts as used in Au+Au collisions were applied. Charged kaon and pion candidates were selected by requiring $|N_{\sigma\pi,K}| < 2$ to reduce the residual background. All other track cuts for both kaon and pion candidates were the same as for Au + Au data.

The $K^{*\pm}$ was measured only in minimum bias $p + p$ interactions and in peripheral 50–80% Au+Au collisions. Daughter pions for the $K^{*\pm}$ reconstruction were required to originate from the interaction point and pass the same cuts as used for the K^{*0} analysis in $p + p$ collisions. The K^0_S was reconstructed by the decay topology method [33,34]. The granddaughter charged pion candidates were selected from global tracks (which do not necessarily originate from the primary collision vertex) with a distance of closest approach to the interaction point greater than 0.5 cm. Candidates for the granddaughter charged pions were also required to have at least 15 hit points in the TPC with $p > 0.2$ GeV/c. Oppositely charged candidates were then paired to form neutral decay vertices. The distance of closest approach for each pair was required to be less than 1.0 cm and the neutral decay vertices were required to be at least 2.0 cm away from the primary vertex to reduce the combinatorial background. The reconstructed K^0_S momentum vector was required to point back to the primary interaction point within 1.0 cm. Only the K^0_S candidates with $\pi^+\pi^-$ invariant mass between 0.48 and 0.51 GeV/c^2 were selected. When the K^0_S candidate was paired with the daughter pion to reconstruct the charged K^*, tracks were checked to avoid double-counting among the three tracks used. Figure 2 shows the K^0_S signal observed in the $\pi^+\pi^-$ invariant mass distribution in $p + p$ collisions. The Gaussian width of this K^0_S signal is around 7 MeV/c^2, which is mainly determined by the momentum resolution of the detector. Because of detector effects, such as the daughter tracks' energy loss in the TPC, the K^0_S mass is shifted by -3 MeV/c^2. The measured K^0_S mass and width agree well with Monte Carlo (MC) simulations, which included the finite momentum resolution of the detector and the daughter tracks' energy loss in the TPC.

The $K\pi$ pairs with their parent rapidity (y) of $|y| < 0.5$ were selected. All the cuts used in this K^* analysis are summarized in Table I. After all the afore mentioned cuts have been applied, a plot of the K^* reconstruction efficiencies multiplied by the detector acceptance can be made (Fig. 9).

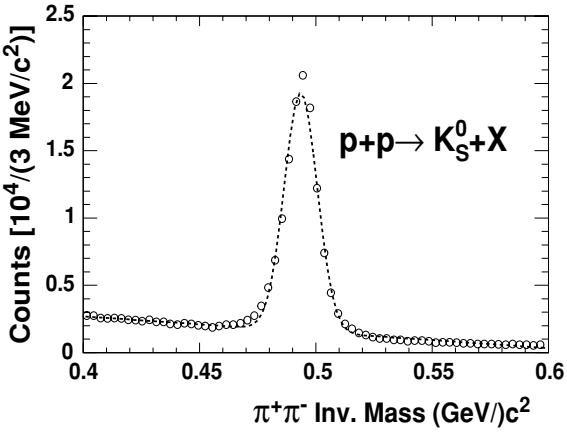

FIG. 2. K^0_S signal observed in the $\pi^+\pi^-$ invariant mass distribution reconstructed from the decay topology method via $K^0_S \to \pi^+\pi^-$ in $p + p$ collisions. The dashed curve depicts the Gaussian fit function plus a linear function representing the background.

IV. EXTRACTION OF THE K^* SIGNAL

In Au+Au collisions, up to several thousand charged tracks per event originate from the primary collision vertex. The daughters from K^* decays are topologically indistinguishable from other primary particles. The measurement was performed by calculating the invariant mass for each $K\pi$ pair in an event. The $K^\pm\pi^\mp$ invariant mass distribution is shown in Fig. 3 as open circles. The unlike-sign $K\pi$ invariant mass distribution derived in this manner was mostly from random $K\pi$ combinatorial pairs. The signal to background is between 1/200 for minimum bias Au+Au and 1/10 for minimum bias $p + p$. The overwhelming combinatorial background distribution can be obtained and subtracted from the unlike-sign $K\pi$ invariant mass distribution in two ways:

- the mixed-event technique, in which the reference background distribution is built with uncorrelated unlike-sign kaons and pions from different events;

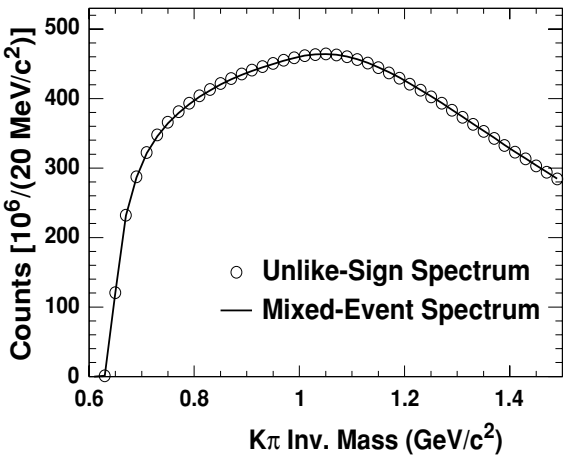

FIG. 3. The unlike-sign $K\pi$ invariant mass distribution (open symbols) and the mixed-event $K\pi$ invariant mass distribution after normalization (solid curve) from minimum bias Au+Au collisions.

TABLE I. List of track cuts for charged kaon and charged pion and topological cuts for neutral kaon used in the K^* analysis in Au+Au and $p+p$ collisions. *decayLength* is the decay length, *dcaDaughters* is the distance of closest approach between the daughters, $dcaV0PrmVx$ is the distance of closest approach between the reconstructed K^0_S momentum vector and the primary interaction vertex, *dcaPosPrmVx* is the distance of closest approach between the positively charged granddaughter and the primary vertex, *dcaNegPrmVx* is the distance of closest approach between the negatively charged granddaughter and the primary vertex, $M_{K^0_S}$ is the K^0_S invariant mass in GeV/c^2, *NFitPnts* is the number of fit points of a track in the TPC, *NTpcHits* is the number of hits of a track in the TPC, *MaxPnts* is the number of maximum possible points of a track in the TPC, and *DCA* is the distance of closest approach to the primary interaction point.

Cuts	K^{*0}		$K^{*\pm}$	
	Au+Au	$p+p$	Daughter $\pi^\pm$	K^0_S
$N_{\sigma K}$	(−2.0, 2.0)	(−2.0, 2.0)		*decayLength* > 2.0 cm
$N_{\sigma\pi}$	(−3.0, 3.0)	(−2.0, 2.0)	(−2.0, 2.0)	*dcaDaughters* < 1.0 cm
Kaon p (GeV/c)	(0.2, 10.0)	(0.2, 0.7)		*dcaV0PrmVx* < 1.0 cm
Kaon p_T (GeV/c)	(0.2, 10.0)	(0.2, 0.7)		*dcaPosPrmVx* > 0.5 cm
Pion p (GeV/c)	(0.2, 10.0)	(0.2, 10.0)	(0.2, 10.0)	*dcaNegPrmVx* > 0.5 cm
Pion p_T (GeV/c)	(0.2, 10.0)	(0.2, 10.0)	(0.2, 10.0)	$M_{K^0_S}$ (GeV/c^2): (0.48, 0.51)
NFitPnts	>15	>15	>15	π^+: *NTpcHits* 15
NFitPnts/*MaxPnts*	>0.55	>0.55	>0.55	π^-: *NTpcHits* 15
Kaon and pion η	$\lvert\eta\rvert < 0.8$	$\lvert\eta\rvert < 0.8$	$\lvert\eta\rvert < 0.8$	π^+: $p > 0.2$ GeV/c
DCA (cm)	<3.0	<3.0	<3.0	π^-: $p > 0.2$ GeV/c
Pair $(K\pi)$ y			$\lvert y\rvert < 0.5$	

- the like-sign technique, in which the reference background distribution is made from like-sign kaons and pions in the same event.

The mixed-event technique has been successfully used in the measurement of resonances at RHIC, such as the $K(892)^{*0}$ in Au+Au collisions at $\sqrt{s_{NN}} = 130$ GeV [35] and the ϕ in Au+Au collisions at $\sqrt{s_{NN}} = 130$ and 200 GeV [36,37]. This technique was also used in the measurement of Λ production in Au+Au collisions at $\sqrt{s_{NN}} = 130$ GeV, and the results agree well with those from the decay topology method [34,38]. The like-sign technique has been successfully applied in measuring $\rho(770)^0 \to \pi^+\pi^-$ production in $p+p$ and peripheral Au+Au collisions at $\sqrt{s_{NN}} = 200$ GeV at RHIC [12].

A. Mixed-event technique

To subtract the uncorrelated pairs from the unlike-sign $K\pi$ invariant mass distribution obtained from the same events, an unlike-sign $K\pi$ invariant mass spectrum from mixed events was obtained. To keep the event characteristics as similar as possible among different events, the whole data sample was divided into 10 bins in charged particle multiplicity and 10 bins in the collision vertex position along the beam direction. Only pairs from events in the same multiplicity and vertex position bins were selected.

In the unlike-sign invariant mass distribution from an event, samples were made from $K_1^+\pi_1^-$ and $K_1^-\pi_1^+$ pairs, which include the desired K^* signal and the background. In the mixed-event spectrum, $K_1^+\pi_i^-$, $K_1^-\pi_i^+$, $K_i^+\pi_1^-$, and $K_i^-\pi_1^+$ pairs were sampled for the background estimation. The subscripts 1 and i correspond to event numbers with $i \neq 1$. The number of events to be mixed was chosen to be 5, so that the total number of entries in the mixed-event invariant mass distribution was ∼10 times that of the total number of entries in the distribution from the same events. Thus the mixed-event spectrum needs to be normalized to subtract the background in the unlike-sign spectrum. Since the $K\pi$ pairs with invariant mass greater than 1.1 GeV/c^2 are less likely to be correlated in the unlike-sign distribution, the normalization factor was calculated by taking the ratio between the number of entries in the unlike-sign and the mixed-event distributions for invariant mass greater than 1.1 GeV/c^2. The solid curve in Fig. 3 corresponds to the mixed-event $K\pi$ pair invariant mass distribution after normalization. The mixed-event distribution was then subtracted from the unlike-sign distribution as follows:

$$N_{K^{*0}}(m) = N_{K_1^+\pi_1^-}(m) + N_{K_1^-\pi_1^+}(m) - R \times \sum_{i=2}^{6} [N_{K_1^+\pi_i^-}(m) + N_{K_1^-\pi_i^+}(m) + N_{K_i^+\pi_1^-}(m) + N_{K_i^-\pi_1^+}(m)], \quad (2)$$

where N is the number of entries in a bin with its center at the $K\pi$ pair invariant mass m and R is the normalization factor. After the mixed-event background subtraction, the K^{*0} signal is visible, as depicted by the open star symbols in Fig. 5.

B. Like-sign technique

The like-sign technique is another approach to subtract the background of noncorrelated pairs from the unlike-sign $K\pi$ invariant mass distribution from the same events. The uncorrelated background in the unlike-sign $K\pi$ distribution was described by using the invariant mass distributions obtained from uncorrelated $K^+\pi^+$ and $K^-\pi^-$ pairs from the same events.

In the unlike-sign $K\pi$ invariant mass spectrum, $K_1^+\pi_1^-$ and $K_1^-\pi_1^+$ pairs were sampled. $K_1^+\pi_1^+$ and $K_1^-\pi_1^-$ pairs were sampled in the like-sign $K\pi$ invariant mass distribution. Since the number of positive and negative particles may not be the same in relativistic heavy-ion collisions, to correctly

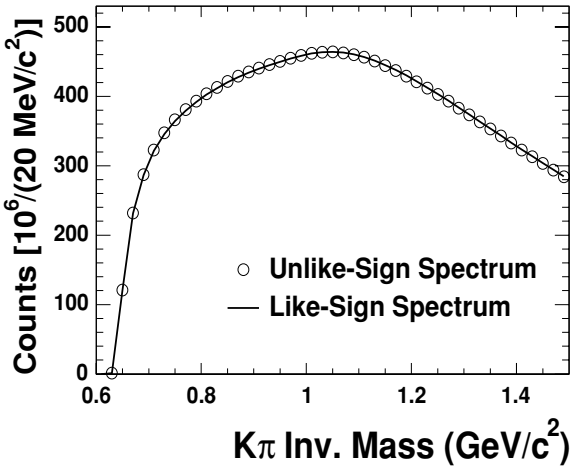

FIG. 4. The unlike-sign $K\pi$ invariant mass distribution (open symbols) and the like-sign $K\pi$ invariant mass distribution (solid curve) from minimum bias Au+Au collisions.

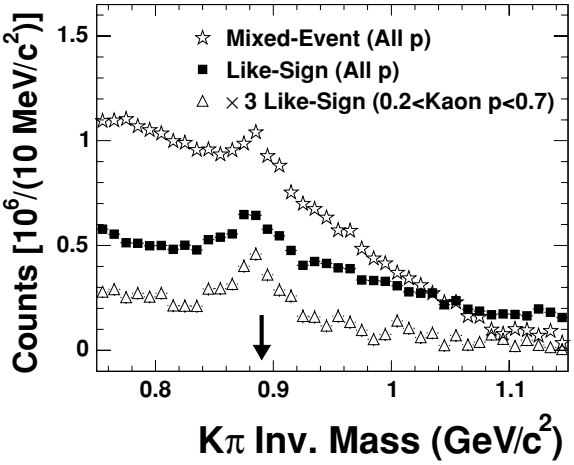

FIG. 5. The $K\pi$ invariant mass distributions after event-mixing background subtraction (open star symbols) and like-sign background subtraction with different daughter momentum cuts ($0.2 <$ kaon and pion $p < 10$ GeV/c for filled square symbols, $0.2 <$ kaon $p <$ 0.7 GeV/c and $0.2 <$ pion $p < 10$ GeV/c for open triangle symbols) demonstrating the sources of the residual background in minimum bias Au+Au collisions. The open triangle symbols have been scaled up by a factor of 3 to increase their visibility. The arrow depicts the standard K^{*0} mass of 896.1 MeV/c^2 [32].

subtract the subset of noncorrelated pairs in the unlike-sign $K\pi$ distribution, the like-sign $K\pi$ invariant mass distribution was calculated as follows:

$$N_{\text{Like-Sign}}(m) = 2 \times \sqrt{N_{K_1^+\pi_1^+}(m) \times N_{K_1^-\pi_1^-}(m)}, \quad (3)$$

where N is the number of entries in a bin with its center at the $K\pi$ pair invariant mass m. The unlike-sign and the like-sign invariant mass distributions are shown in Fig. 4. The like-sign spectrum was then subtracted from the unlike-sign distribution:

$$N_{K^{*0}}(m) = N_{K_1^+\pi_1^-}(m) + N_{K_1^-\pi_1^+}(m) - N_{\text{Like-Sign}}(m). \quad (4)$$

The like-sign, background-subtracted $K\pi$ invariant mass distribution corresponds to the solid square symbols in Fig. 5, where the K^{*0} signal is now visible.

Compared to the mixed-event technique, the like-sign technique has the advantage that the unlike-sign and like-sign pairs are taken from the same event, so there is no event structure difference between the two distributions resulting from effects such as elliptic flow. The short-coming of this technique is that the like-sign distribution has larger statistical uncertainties compared to the mixed-event spectrum, since the statistics in the mixed-event and like-sign techniques are driven by the number of events mixed and the number of kaons and pions produced per event, respectively [39]. Therefore, in this analysis, the mixed-event technique was used to reconstruct the K^* signal whereas the like-sign technique was used to study the sources of the residual background under the K^{*0} peak after mixed-event background subtraction, as discussed in details in the following text.

C. Describing the residual background

The unlike-sign $K\pi$ invariant mass distribution after mixed-event background subtraction is represented by the open star symbols in Fig. 5, where the K^{*0} signal is clearly observed. The mixed-event technique removes only the uncorrelated background pairs in the unlike-sign spectrum. As a consequence, residual correlations near the K^{*0} mass range were not subtracted by the mixed-event spectrum. This residual background may come from three dominant sources:

- elliptic flow in noncentral Au + Au collisions,
- correlated real $K\pi$ pairs, or
- correlated but misidentified pairs.

The overlapping region of noncentral Au+Au collisions has an elliptic shape in the plane perpendicular to the beam axis. Each noncentral Au+Au event has a unique reaction plane angle. The azimuthal distributions for kaons and pions may be different for different events. Thus, the unlike-sign $K\pi$ pair invariant mass spectrum may have a different structure than the mixed-event invariant mass distribution. This structural difference may lead to a significant residual background in the unlike-sign $K\pi$ invariant mass spectrum after mixed-event background subtraction [40].

In the like-sign technique, the unlike-sign $K\pi$ spectrum and the like-sign distribution are obtained from the same events. Therefore, no correlations resulting from elliptic flow should be present in the unlike-sign $K\pi$ invariant mass spectrum after like-sign background subtraction. In Fig. 5, the solid square symbols represent the unlike-sign $K\pi$ invariant mass distribution after like-sign background subtraction. The amplitude of the residual background below the peak after the like-sign background subtraction is about a factor of 2 smaller than that after the mixed-event background subtraction, whereas the amplitude of the K^{*0} signal remains the same. This indicates that part of the residual background in the spectrum after mixed-event background subtraction was induced by elliptic azimuthal anisotropy.

In the K^{*0} analysis in Au+Au collisions, since the kaons and pions are selected with $0.2 < p < 10.0$ GeV/c, a pion

(kaon) with $p > 0.75$ GeV/c may be misidentified as a kaon (pion). A proton with $p > 1.1$ GeV/c may be misidentified as either a kaon or a pion, or both, depending on whether kaons or pions are being selected. Electrons and positrons that cross the kaon (pion) band in the dE/dx plot shown in Fig. 1 may be misidentifed as kaons (pions). Thus, the daughters from $\rho^0 \to \pi^+\pi^-$, $\phi \to K^+K^-$, $\Lambda \to \pi^- p$, etc. could be falsely identified as a $K\pi$ pair if the daughter momenta are beyond the particle identification range. The invariant mass calculated from these misidentified pairs cannot be subtracted away by the mixed-event background and remains as part of the residual background.

In Fig. 5, the open triangle symbols correspond to the unlike-sign $K\pi$ spectrum after like-sign background subtraction with $0.2 < p < 0.7$ GeV/c and $0.2 < p < 10.0$ GeV/c for the kaon and the pion, respectively. These momentum cuts allow only correlated $K\pi$ real pairs and pairs in which a kaon or a proton was misidentified as a pion to contribute to the background-subtracted spectrum. Compared to the solid square symbols in Fig. 5, the residual background represented by the open triangle symbols is reduced by a factor of 6 and the K^{*0} signal is a factor of 2 smaller. This indicates that particle misidentification of the decay products of ρ, ω, η, K^0_S, Λ, etc. indeed causes false correlations to appear in the background-subtracted distribution.

Correlated real $K\pi$ pairs from real particle decays—such as higher mass resonant states in the K–π system and particle decay modes with three or more daughters where two of them are a $K\pi$ pair—as well as the nonresonant K–π s-wave correlation-also contribute to the unlike-sign $K\pi$ spectrum. These correlated $K\pi$ pairs contribute to the residual background, since they are not present in the like-sign and mixed-event distributions. There is no efficient cut to remove these real correlations from the residual background.

V. ANALYSIS AND RESULTS

A. K^{*0} mass and width

Figure 6 depicts the mixed-event, background-subtracted $K\pi$ invariant mass distributions ($M_{K\pi}$) integrated over the K^* p_T for central Au+Au (upper panel) and for minimum bias $p + p$ (lower panel) interactions. The mass of the K^{*0} was fit to the function

$$\mathrm{BW} \times \mathrm{PS} + \mathrm{RBG}, \tag{5}$$

where BW is the relativistic p-wave Breit-Wigner function [41] given by

$$\mathrm{BW} = \frac{M_{K\pi}\Gamma M_0}{\left(M^2_{K\pi} - M^2_0\right)^2 + M^2_0\Gamma^2}, \tag{6}$$

PS is the Boltzmann factor [7,8,15,16] given by

$$\mathrm{PS} = \frac{M_{K\pi}}{\sqrt{M^2_{K\pi} + p^2_T}} \times \exp\left(-\frac{\sqrt{M^2_{K\pi} + p^2_T}}{T_{\mathrm{fo}}}\right), \tag{7}$$

which accounts for phase space, and the linear function

$$\mathrm{RBG} = a + bM_{K\pi} \tag{8}$$

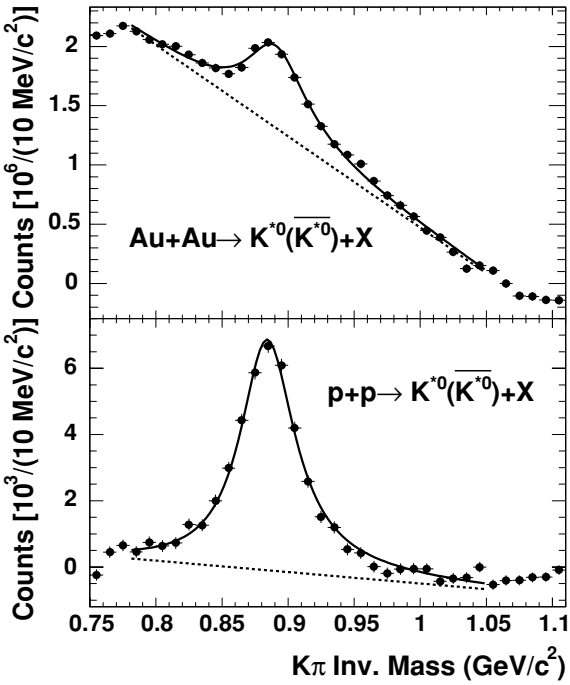

FIG. 6. The $K\pi$ invariant mass distribution integrated over the K^* p_T for central Au+Au (upper panel) and minimum bias $p + p$ (lower panel) interactions after the mixed-event background subtraction. The solid curves are the fits to Eq. (5) with $T_{\mathrm{fo}} = 120$ MeV and $p_T = 1.8$ GeV/c for central Au+Au and $T_{\mathrm{fo}} = 160$ MeV and $p_T = 0.8$ GeV/c for $p + p$, respectively. The dashed lines are the linear functions representing the residual background.

represents the residual background. Within this parametrization, T_{fo} is the temperature at which the resonance is emitted [8] and

$$\Gamma = \frac{\Gamma_0 M^4_0}{M^4_{K\pi}} \times \left[\frac{\left(M^2_{K\pi} - M^2_\pi - M^2_K\right)^2 - 4M^2_\pi M^2_K}{\left(M^2_0 - M^2_\pi - M^2_K\right)^2 - 4M^2_\pi M^2_K}\right]^{3/2} \tag{9}$$

is the momentum-dependent width [41]. In addition, M_0 is the K^* mass, Γ_0 is the K^* width, p_T is the K^* transverse momentum, M_π is the pion mass, and M_K is the kaon mass.

The PS factor accounts for K^* produced through kaon and pion scattering, or $K + \pi \to K^* \to K + \pi$. In Au + Au collisions, the thermal freeze-out temperature $T_{\mathrm{fo}} = 90$ MeV was measured at STAR [42]. However, resonances can be produced over a range of temperature inside the hadronic system and not all resonances are emitted at the point where the system freezes out at $T_{\mathrm{fo}} = 90$ MeV. As a result, the temperature chosen in the PS factor was 120 MeV according to [8]. The temperature of $T_{\mathrm{fo}} = 90$ MeV was also used to estimate the systematic uncertainties, which are about 1.5 MeV/c^2 for masses and 5 MeV/c^2 owing to the choice of T_{fo}. In $p + p$ collisions, particle production is well reproduced by the statistical model [43] with $T_{\mathrm{fo}} = 160$ MeV and therefore this was the temperature used in the PS factor. Values of $p_T = 1.8$ GeV/c and 0.8 GeV/c were chosen in the PS factor for the Au+Au and $p + p$ collisions, respectively, which are

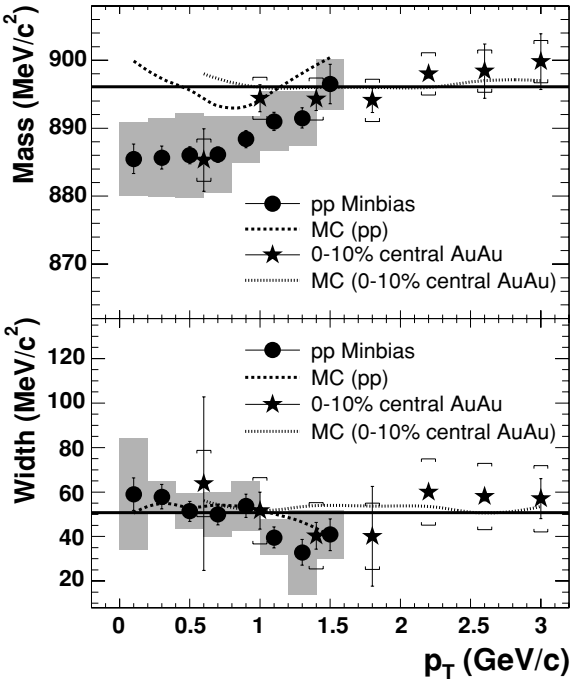

FIG. 7. The K^{*0} mass (upper panel) and width (lower panel) as a function of p_T for minimum bias $p+p$ interactions and for central Au+Au collisions. The solid straight lines are the standard K^{*0} mass (896.1 MeV/c^2) and width (50.7 MeV/c^2) [32], respectively. The dashed and dotted curves are the MC results in minimum bias $p+p$ and for central Au+Au collisions, respectively, after considering detector effects and kinematic cuts. The gray shadows (caps) indicate the systematic uncertainties for the measurement in minimum bias $p+p$ interactions (central Au+Au collisions).

the centers of the entire measured p_T ranges ($0.4 < p_T < 3.2$ GeV/c for Au+Au and $p_T < 1.6$ GeV/c for $p+p$).

Mixed-event, background-subtracted $K\pi$ invariant mass distributions were obtained for different p_T bins, and each p_T bin was fit to Eq. (5) with the K^{*0} mass, width, and uncorrected yield as free parameters. The χ^2/ndf of the fit varies between 0.6 and 1.7 for all p_T bins except for two p_T bins (3.8 for the $2.0 < p_T < 2.4$ GeV/c bin and 2.6 for the $2.4 < p_T < 2.8$ GeV/c bin) in the central Au+Au data, where the uncertainties of the mass and width values are not well constrained. Figure 7 shows the K^{*0} mass (upper panel) and width (lower panel) for central Au+Au and for minimum bias $p+p$ interactions as a function of the K^{*0} p_T. Monte carlo calculations for the K^{*0} mass and width were obtained by simulating K^{*0} with standard mass and width values [32] and passing them through the same reconstruction steps and kinematic cuts as the real data. The results from such simulations are also depicted in Fig. 7. The deviations between the MC results and the standard mass and width values are mainly due to the kinematic cuts (track p and p_T cuts, etc.). For example, the $p_T > 0.2$ GeV/c cut results in the rise of the mass at low p_T and the kaon $p < 0.7$ GeV/c cut in $p+p$ causes the rise of the mass and the drop of the width at higher p_T. Our MC studies indicate that the deviations induced by kinematic cuts are not sufficient to explain the mass shift seen in the data.

The systematic uncertainties in the K^{*0} mass and width for the measurement in minimum bias $p+p$ interactions were evaluated bin by bin by varying the particle types (either K^{*0} or $\overline{K^{*0}}$), the methods in the background subtraction (mixed-event or like-sign), the residual background functions (exponential or second-order polynomial functions), the dynamical cuts, and the track types (primary tracks or global tracks) and by considering the detector effects (different TPC magnetic field directions, different sides of the TPC detector, etc.). Because of the limited statistics, the systematic uncertainties (3.1 MeV/c^2 for masses and 14.9 MeV/c^2 for widths) in central Au+Au interactions were only estimated using the entire measured p_T range ($0.4 < p_T < 3.2$ GeV/c) following these steps. More detailed discussions about the systematic uncertainty studies can be found in [39]. In minimum bias $p+p$ interactions, the K^{*0} masses at low p_T (first 2 or 3 data points) are lower than the MC results at a 2- to 3-σ level.

B. m_T and p_T spectra

Mixed-event, background-subtracted $K\pi$ invariant mass distributions were obtained for different p_T bins, and each p_T bin was fit to the function

$$\mathrm{SBW} + \mathrm{RBG}, \tag{10}$$

where SBW is the nonrelativistic Breit-Wigner function [32] given by

$$\mathrm{SBW} = \frac{\Gamma_0}{(M_{K\pi} - M_0)^2 + \Gamma_0^2/4} \tag{11}$$

and RBG is the linear function from Eq. (8) that represents the residual background. The fit sensitivity to statistical fluctuations in the K^* raw yield was reduced by fixing the mass and width in the fit according to the values obtained from the free parameter fit with the same simplified BW function. The χ^2/ndf of the fit varies between 0.7 and 1.8 for all p_T bins except for two p_T bins ($\sim$3.0 for the $2.0 < p_T < 2.4$ GeV/c bin and $\sim$2.7 for the $2.4 < p_T < 2.8$ GeV/c bin) in Au+Au data. The K^* raw yield was also obtained by fitting the data to the BW function from Eq. (6) with all parameters free in the fit. The difference in the raw yields between the two fit functions was included in the systematic uncertainties. The $K^0_S\pi^\pm$ invariant mass distribution fit to Eq. (10) after the mixed-event background subtraction is shown in Fig. 8 for minimum bias $p+p$ collisions (upper panel) and for the 50–80% of the inelastic hadronic Au+Au cross section (lower panel).

About 6×10^6, 2×10^6, and 5.6×10^4 K^{*0} signals were reconstructed from top 10% central Au+Au, minimum bias Au+Au, and minimum bias $p+p$ collisions, respectively, whereas about 1.2×10^4 and 10^4 $K^{*\pm}$ were observed in the 50–80% Au+Au and minimum bias $p+p$ collisions, respectively. The K^{*0} and $K^{*\pm}$ raw yields obtained for different p_T bins in Au+Au and minimum bias $p+p$ collisions were then corrected for the detector acceptance and efficiency (shown in Fig. 9) determined from a detailed simulation of the TPC response using GEANT [44]. The corresponding branching ratios were also taken into account. In addition, the yields in

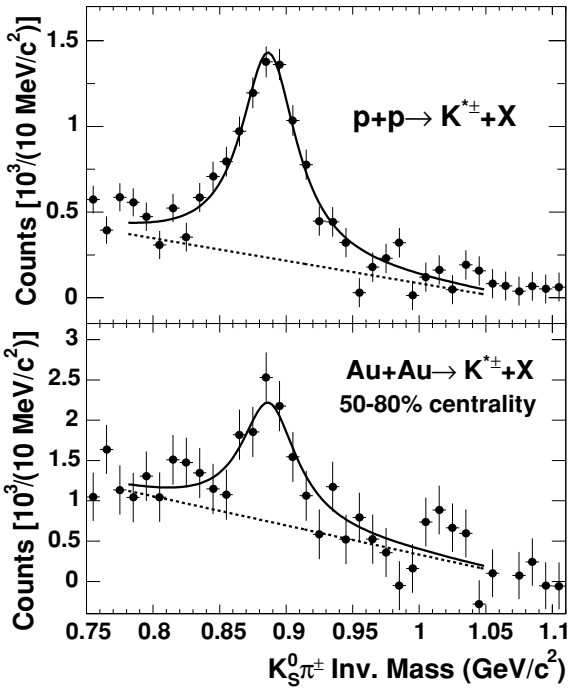

FIG. 8. The $K^0_S\pi^\pm$ invariant mass distribution integrated over the $K^{*\pm}$ p_T for minimum bias $p+p$ collisions (upper panel) and for the 50–80% of the inelastic hadronic Au+Au cross section (lower panel) after the mixed-event background subtraction. The solid curves are fits to Eq. (10) and the dashed lines are the linear function representing the residual background.

$p+p$ were corrected for the collision vertex finding efficiency of 86%.

The transverse mass (m_T) distributions of the midrapidity $(K^{*0}+\overline{K^{*0}})/2$ invariant yields in central Au+Au, four different centralities in minimum bias Au+Au, and minimum bias $p+p$ collisions are depicted in Fig. 10. The $(K^{*+}+K^{*-})/2$ invariant yields for the most peripheral 50–80% Au+Au collisions are also shown for comparison. The K^{*0} invariant yield $[d^2N/(2\pi m_T dy dm_T)]$ distributions were fit to

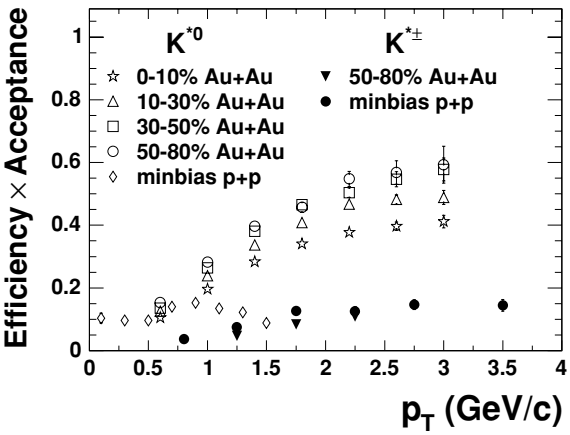

FIG. 9. The K^{*0} and $K^{*\pm}$ reconstruction efficiency multiplied by the detector acceptance as a function of p_T in minimum bias $p+p$ and different centralities in Au+Au collisions.

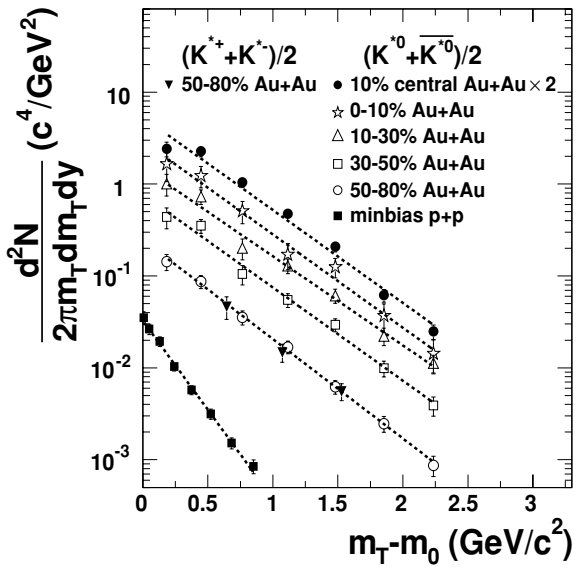

FIG. 10. The $(K^*+\overline{K^*})/2$ invariant yields as a function of $m_T - m_0$ for $|y|<0.5$ from minimum bias $p+p$ and different centralities in Au+Au collisions. The top 10% central data have been multiplied by 2 for clarity. The lines are fits to Eq. (12). The errors shown are the quadratic sum of statistical and systematic (at the level of 10%) uncertainties.

the following exponential function:

$$\frac{1}{2\pi m_T}\frac{d^2N}{dy\,dm_T} = \frac{dN}{dy}\frac{1}{2\pi T(m_0+T)}\exp\left(\frac{-(m_T-m_0)}{T}\right), \tag{12}$$

where dN/dy is the K^{*0} yield at $|y|<0.5$ and T is the inverse slope parameter. The extracted dN/dy and T parameters are listed in Table II. The systematic uncertainties on the K^{*0} dN/dy and T in Au+Au and $p+p$ collisions were estimated by comparing different Breit-Wigner functions, particle types (either K^{*0} or $\overline{K^{*0}}$), residual background functions (exponential or second-order polynomial functions), and dynamical cuts and by considering the detector effects. More detailed discussions about the systematic uncertainty studies can be found in [39]. The K^{*0} invariant yield increases from $p+p$ collisions to peripheral Au+Au and to central

TABLE II. The K^{*0} dN/dy and T for $|y|<0.5$ from central Au+Au, four different centralities in minimum bias Au+Au, and minimum bias $p+p$ collisions. The first error is statistical; the second is systematic.

	dN/dy	T (MeV)
Top 10% central	$10.18 \pm 0.46 \pm 1.88$	$427 \pm 10 \pm 46$
0–10%	$10.48 \pm 1.45 \pm 1.94$	$428 \pm 31 \pm 47$
10–30%	$5.86 \pm 0.56 \pm 1.08$	$446 \pm 23 \pm 49$
30–50%	$2.81 \pm 0.25 \pm 0.52$	$427 \pm 18 \pm 46$
50–80%	$0.82 \pm 0.06 \pm 0.15$	$402 \pm 14 \pm 44$
$p+p$	$(5.08 \pm 0.17 \pm 0.61)\times 10^{-2}$	$223 \pm 8 \pm 9$

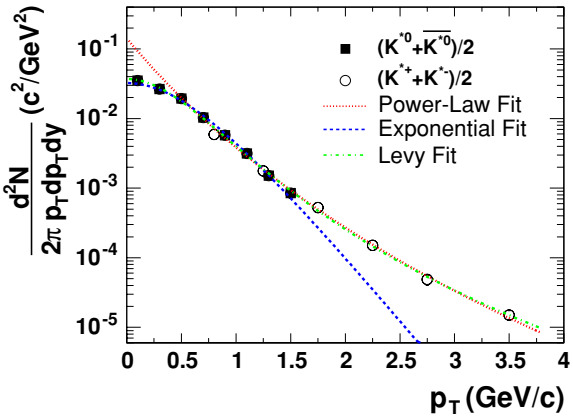

FIG. 11. (Color online) The invariant yields for both $(K^{*0} + \overline{K^{*0}})/2$ and $(K^{*+} + K^{*-})/2$ as a function of p_T for $|y| < 0.5$ in minimum bias $p + p$ interactions. The dotted curve is the fit to the power-law function from Eq. (13) for $p_T > 0.5$ GeV/c and extended to lower values of p_T. The dashed curve is the K^{*0} spectrum fit to the exponential function from Eq. (12) and extended to higher values of p_T. The dashed-dotted curve is the fit to the Levy function from Eq. (14) for $p_T < 4$ GeV/c. Errors are statistical only.

Au+Au collisions. The inverse slope of the K^{*0} spectra for all centrality bins of Au+Au collisions is significantly larger than in minimum bias $p + p$ collisions.

Theoretical calculations [45] indicate that, in $p + p$ collisions, particle production is dominated by hard processes for p_T above 1.5 GeV/c whereas soft processes dominate at low p_T. Thus in the K^* p_T spectrum, a power-law shape for p_T above 1.5 GeV/c and an exponential shape at lower p_T should be expected. In minimum bias $p + p$ collisions, owing to the cut on the kaon daughter of $p < 0.7$ GeV/c, only the K^{*0} spectrum for $p_T < 1.6$ GeV/c was measured. As a result, the K^{*0} m_T spectrum in minimum bias $p + p$ collisions can be well described by the commonly used exponential function, as shown in Fig. 10. The K^* p_T spectrum can be extended to higher p_T by measuring the $K^{*\pm}$ signals. Figure 11 shows the $(K^{*0} + \overline{K^{*0}})/2$ and $(K^{*+} + K^{*-})/2$ invariant yields for $|y| < 0.5$ as a function of p_T. The dotted curve in this figure is the fit to the power-law function

$$\frac{1}{2\pi p_T}\frac{d^2N}{dy\,dp_T} = \frac{dN}{dy}\frac{2(n-1)(n-2)}{\pi(n-3)^2\langle p_T\rangle^2} \times \left(1 + \frac{p_T}{\langle p_T\rangle(n-3)/2}\right)^{-n}, \quad (13)$$

where n is the order of the power law and $\langle p_T\rangle$ is the average transverse momentum. The data were fit for $p_T > 0.5$ GeV/c. The power-law fit does not reproduce the two first p_T bins (0.0 $p_T < 0.2$ GeV/c and 0.2 $p_T < 0.4$ GeV/c) since at low p_T particle production may be dominated by soft processes. From the power-law fit, the χ^2/ndf is 0.93. The dashed curve in Fig. 11 is the K^{*0} spectrum fit to the exponential function from Eq. (12) and then extrapolated to higher p_T. The data could not be described by this exponential fit, indicating that hard processes dominate the particle production for $p_T > 1.5$ GeV/c. In some models [46] it is suggested that one use the following Levy function to represent the p_T spectrum:

$$\frac{1}{2\pi p_T}\frac{d^2N}{dy dp_T} = \frac{dN}{dy}\frac{(n-1)(n-2)}{2\pi nT[nT + m_0(n-2)]} \times \left(1 + \frac{\overline{p_T^2 + m_0^2} - m_0}{nT}\right)^{-n}. \quad (14)$$

The dashed-dotted curve in Fig. 11 is the Levy function fit with $\chi^2/ndf = 0.90$ to the K^* spectrum in all the measured p_T range ($p_T < 4$ GeV/c).

TABLE III. The K^* $\langle p_T\rangle$ for different centralities in Au+Au and minimum bias $p + p$ collisions. The first error is statistical; the second is systematic.

	$\langle p_T\rangle$ (GeV/c)
Top 10% central	$1.08 \pm 0.03 \pm 0.12$
0–10%	$1.08 \pm 0.08 \pm 0.12$
10–30%	$1.12 \pm 0.06 \pm 0.13$
30–50%	$1.08 \pm 0.05 \pm 0.12$
50–80%	$1.03 \pm 0.04 \pm 0.12$
$p + p$	$0.81 \pm 0.02 \pm 0.14$

C. Average transverse momentum $\langle p_T\rangle$

In Au + Au collisions, the p_T range of the exponential fit covers >85% of all the K^* yield so that the K^* average transverse momentum ($\langle p_T\rangle$) can be reasonably calculated by using the inverse slope parameter (T) extracted from the exponential fit function and assuming the exponential behavior over all the p_T range:

$$\langle p_T\rangle = \frac{\int_0^\infty p_T^2 e^{-(\sqrt{p_T^2+m_0^2}-m_0)/T}dp_T}{\int_0^\infty p_T e^{-(\sqrt{p_T^2+m_0^2}-m_0)/T}dp_T}.$$

In $p + p$ collisions, the neutral and charged K^* spectrum shown in Fig. 11 covers >98% of all the K^* yield so that $\langle p_T\rangle$ is directly calculated from the data points in the spectrum. The systematic uncertainty in $p + p$ includes the differences between this calculation and the exponential fit to the K^{*0} only at $p_T < 1.6$ GeV/c, the power-law fit to both neutral and charged K^* at $p_T > 1.5$ GeV/c, and the Levy function fit at $p_T < 4$ GeV/c. The systematic uncertainties for all the $\langle p_T\rangle$ values include the effects discussed in the previous section and the differences caused by different fit functions to the invariant yield, such as the Boltzmann fit ($m_T e^{-(m_T-m_0)/T}$) and the blast wave model fit [47]. The calculated K^* $\langle p_T\rangle$ for different centralities in Au+Au and minimum bias $p + p$ collisions are listed in Table III.

The K^* $\langle p_T\rangle$ as a function of the charged particle multiplicity ($dN_{\rm ch}/d\eta$) is shown in Fig. 12 and is compared to that of π^-, K^-, and $\overline{p}$ [42] for different centralities in Au+Au and minimum bias $p + p$ collisions. The K^{*0} $\langle p_T\rangle$ in Au+Au collisions is significantly larger than in minimum bias

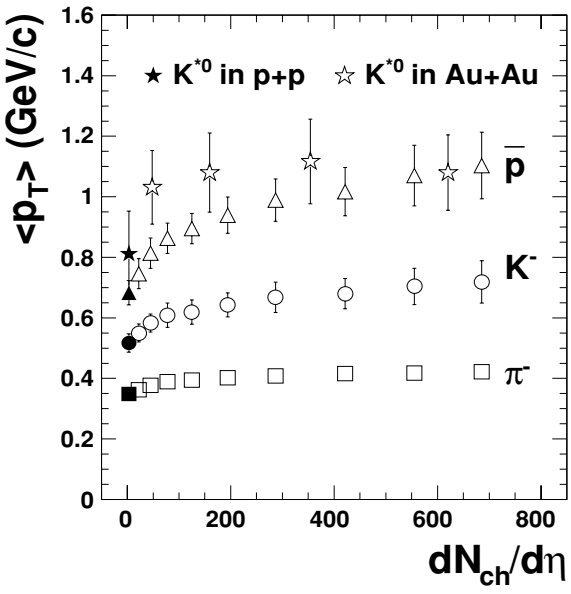

FIG. 12. The K^* $\langle p_T \rangle$ as a function of $dN_{\rm ch}/d\eta$ compared to that of π^-, K^-, and $\overline{p}$ for minimum bias $p + p$ (solid symbols) and Au+Au (open symbols) collisions. The errors shown are the quadratic sum of the statistical and systematic uncertainties.

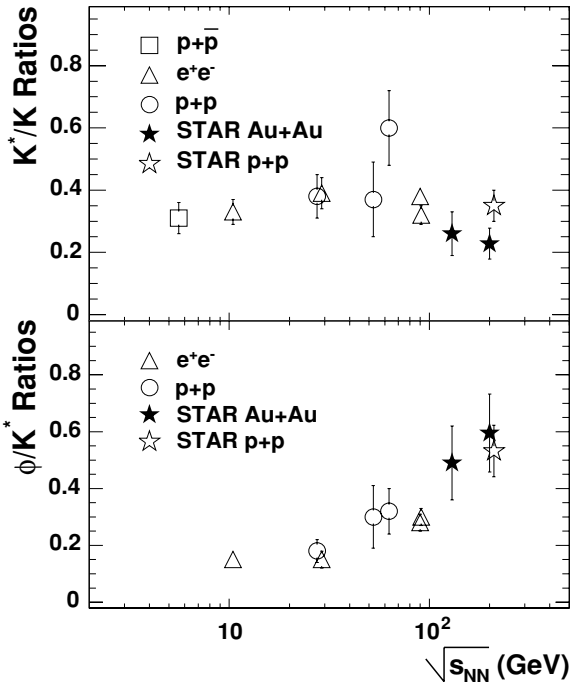

FIG. 13. The K^*/K (upper panel) and ϕ/K^* (lower panel) yield ratios as a function of the c.m. system energies. The yield ratios for central Au+Au collisions at $\sqrt{s_{NN}} = 130$ [35] and 200 GeV and minimum bias $p + p$ interactions at $\sqrt{s_{NN}} = 200$ GeV are compared to measurements from e^+e^- at $\sqrt{s}$ of 10.45 GeV [48], 29 GeV [49] and 91 GeV [50,51], $\bar{p}p$ at $\sqrt{s}$ of 5.6 GeV [52], and pp at $\sqrt{s}$ of 27.5 GeV [53], 52.5 GeV [54], and 63 GeV [55]. The errors at $\sqrt{sNN} = 130$ and 200 GeV correspond to the quadratic sum of the statistical and systematic errors.

$p + p$ collisions. No significant centrality dependence of $\langle p_T \rangle$ is observed for K^* in Au+Au collisions.

D. Particle ratios

The K^* vector meson and its corresponding ground state, the K, have identical quark content in the context of the standard model of particles. They differ only in their masses and the relative orientation of their quark spins. Thus, the K^*/K yield ratio may be the most interesting and the least model dependent ratio for studying the K^* production properties and the freeze-out conditions in relativistic heavy-ion collisions. The K^* and ϕ mesons have a very small mass difference, their total spin difference is $\Delta S = 0$, and both are vector mesons. One significant difference between the K^* and ϕ is their lifetimes, with the ϕ meson lifetime being a factor of 10 longer than that of the K^*. Therefore, it is important to measure the ϕ/K^* yield ratio and compare the potential differences in K^*/K and ϕ/K yield ratios in relativistic heavy-ion collisions to study different hadronic interaction effects on different resonances.

The K^*/K yield ratios as a function of the c.m. system energies are shown in the upper panel of Fig. 13. The K^*/K^- yield ratios for central Au+Au collisions at $\sqrt{s_{NN}} = 130$ [35] and 200 GeV and minimum bias $p + p$ interactions at $\sqrt{s_{NN}} = 200$ GeV are compared to measurements in e^+e^- [48–51], $\overline{p} + p$ [52], and $p + p$ [53–55]. The K^*/K^- yield ratios depicted in Fig. 13 do not show a strong dependence on the colliding system or the c.m. system energy, with the exception of the K^*/K^- yield ratio at $\sqrt{s_{NN}} = 200$ GeV. In this case, the K^*/K^- yield ratio for central Au+Au collisions is significantly lower than the minimum bias $p + p$ measurement at the same c.m. system energy. The ϕ/K^* yield ratios as a function of the c.m. system energies are depicted in the lower panel of Fig. 13. The ϕ/K^* yield ratios for central Au+Au collisions at $\sqrt{s_{NN}} = 130$ [35] and 200 GeV and minimum bias $p + p$ interactions at $\sqrt{s_{NN}} = 200$ GeV are compared to measurements in e^+e^- [48–51] and $p + p$ [53–55]. Figure 13 shows an increase of the yield ratio ϕ/K^* measured in Au+Au collisions compared to the measurements in $p + p$ and e^+e^- at lower energies.

Table IV lists the K^*/K^-, ϕ/K^*, and ϕ/K^- yield ratios for different centralities in Au+Au and minimum bias $p + p$ interactions. Figure 14 depicts the K^*/K^-, ϕ/K^- [37], and ρ^0/π^- [12] yield ratios as a function of $dN_{\rm ch}/d\eta$ at $\sqrt{s_{NN}} = 200$ GeV. All yield ratios have been normalized to the corresponding yield ratio measured in minimum bias $p + p$ collisions at the same $\sqrt{s_{NN}}$ and are indicated by the solid line in Fig. 14. As mentioned previously and shown in Fig. 13, the K^{*0}/K^- yield ratio for central Au+Au collisions is significantly lower than the minimum bias $p + p$ measurement at the same c.m. system energy. In addition, the statistical model prediction of K^*/K of 0.33 ± 0.01 [7,17,56] is considerably larger (in a 2-σ effect) than than our measurement of 0.23 ± 0.05 in 0–10% Au+Au. The K^{*0} regeneration depends on $\sigma_{K\pi}$ whereas the rescattering of the daughter particles depends on $\sigma_{\pi\pi}$ and $\sigma_{\pi p}$, which are considerably larger (factor ∼5) than $\sigma_{K\pi}$ [22,23]. The lower K^{*0}/K^- yield ratio measured may be due to the rescattering of the K^{*0} decay

TABLE IV. The K^*/K^-, ϕ/K^*, and ϕ/K^- yield ratios for different centralities in Au+Au and for minimum bias $p+p$ interactions. The first error is statistical; the second is systematic.

	K^*/K	ϕ/K^*	ϕ/K
0–5%			$0.16 \pm 0.01 \pm 0.02$
0–10%	$0.23 \pm 0.01 \pm 0.05$	$0.60 \pm 0.06 \pm 0.12$	$0.15 \pm 0.01 \pm 0.02$
10–30%	$0.24 \pm 0.02 \pm 0.05$	$0.63 \pm 0.07 \pm 0.14$	$0.16 \pm 0.01 \pm 0.02$
30–50%	$0.26 \pm 0.02 \pm 0.06$	$0.58 \pm 0.06 \pm 0.13$	$0.16 \pm 0.01 \pm 0.02$
50–80%	$0.26 \pm 0.02 \pm 0.05$	$0.53 \pm 0.05 \pm 0.11$	$0.15 \pm 0.01 \pm 0.02$
$p+p$	$0.35 \pm 0.01 \pm 0.05$	$0.53 \pm 0.03 \pm 0.09$	$0.14 \pm 0.01 \pm 0.02$

products. The ρ^0/π^- yield ratio from minimum bias $p+p$ and peripheral Au+Au interactions at the same c.m. system energy are comparable. Owing to the relatively long lifetime of the ϕ meson and the negligible σ_{KK}, the rescattering of the ϕ decay products and the ϕ regeneration should be negligible. The statistical model calculations [17,56] predict the ϕ/π^- yield ratio to be 0.025 ± 0.001 whereas STAR measured the K^-/π^- yield ratio to be 0.15 ± 0.02 [42]. Thus the ϕ/K^- yield ratio combining the model prediction and experimental measurements is 0.17 ± 0.02, which successfully reproduces the ϕ/K^- yield ratio measurement depicted in Table IV and Fig. 14.

The centrality dependence of the resonance yield ratios depicted in Fig. 14 suggests that the ϕ regeneration and the rescattering of the ϕ decay products are negligible, and the rescattering of the K^{*0} decay products is dominant over the K^{*0} regeneration and therefore the reaction channel $K^* \leftrightarrow K\pi$ is not in balance. As a result, the K^{*0}/K^- yield ratio can be used to estimate the time between chemical and kinetic freeze-outs:

$$\left.\frac{K^*}{K}\right|_{\text{kinetic}} = \left.\frac{K^*}{K}\right|_{\text{chemical}} \times e^{-\Delta t/\tau}, \tag{15}$$

where τ is the K^* lifetime of 4 fm/c and Δt is the time between chemical and kinetic freeze-outs. If we use the minimum bias

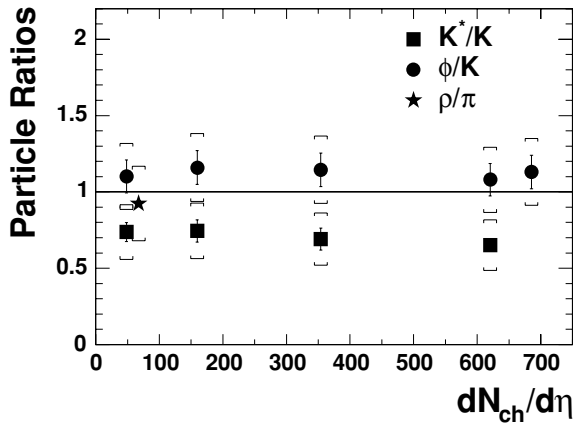

FIG. 14. The K^*/K^-, ϕ/K^-, and ρ^0/π^- yield ratios as a function of $dN_{\text{ch}}/d\eta$ for Au+Au collisions at $\sqrt{s_{NN}} = 200$ GeV. All yield ratios have been normalized to the corresponding yield ratio measured in minimum bias $p+p$ collisions at the same c.m. system energy and are indicated by the solid line. Both statistical and systematic uncertainties are shown.

$p+p$ measurement of the K^{*0}/K^- yield ratio as the one at chemical freeze-out and use the most central measurement of the K^{*0}/K^- yield ratio in Au+Au collisions for the production at kinetic freeze-out, then under the assumptions that (i) all the K^*s that decay before kinetic freeze-out are lost as a result of the rescattering effect and that (ii) no regeneration effect is present, the time between chemical and kinetic freeze-outs is short and $\Delta t = 2 \pm 1$ fm/c. These assumptions reduce the estimated Δt. Thus the previous value is a lower limit of Δt and it is not in conflict with the estimations (>6 fm/c) in [42]. These two measurements together indicate that a considerable resonance regeneration effect may happen even (about 4 fm/c) after chemical freeze-out.

E. Elliptic anisotropy v_2

In noncentral Au+Au collisions, the elliptic flow (v_2) is defined as the second harmonic coefficient of the Fourier expansion of the azimuthal particle distributions in momentum space [57]. The K^{*0} v_2 can be calculated as

$$v_2 = \langle \cos[2(\phi - \Psi_r)] \rangle, \tag{16}$$

where ϕ is the K^{*0} azimuthal angle in the momentum space, Ψ_r denotes the actual reaction plane angle, and $\langle\rangle$ indicates the average over all K^{*0} in all events.

For each $K\pi$ pair, the reaction plane angle was estimated by the event plane (Ψ_2), which in turn was determined by using all the primary tracks except the kaon and pion tracks in the pair:

$$\Psi_2 = \frac{1}{2}\tan^{-1} \times \left(\frac{\sum_i \omega_i \sin(2\phi_i) - \omega_K \sin(2\phi_K) - \omega_\pi \sin(2\phi_\pi)}{\sum_i \omega_i \cos(2\phi_i) - \omega_K \cos(2\phi_K) - \omega_\pi \cos(2\phi_\pi)} \right), \tag{17}$$

where ω_i is the weight for each track used to optimize the event plane resolution and the subscripts K and π stand for the kaon and pion candidate track, respectively. This prevents the autocorrelation between the $K\pi$ azimuthal angle $\phi_{K\pi}$ and the event plane angle Ψ_2 [39].

In minimum bias Au+Au collisions, the unlike-sign and mixed-event $K\pi$ pair invariant mass distributions are reconstructed in $\cos[2(\phi - \Psi_2)]$ bins and in p_T bins. After the mixed-event background subtraction for each $\cos[2(\phi - \Psi_2)]$ bin and p_T bin, the K^{*0} yields are then obtained as a function of $\cos[2(\phi - \Psi_2)]$ for given p_T bin. The average

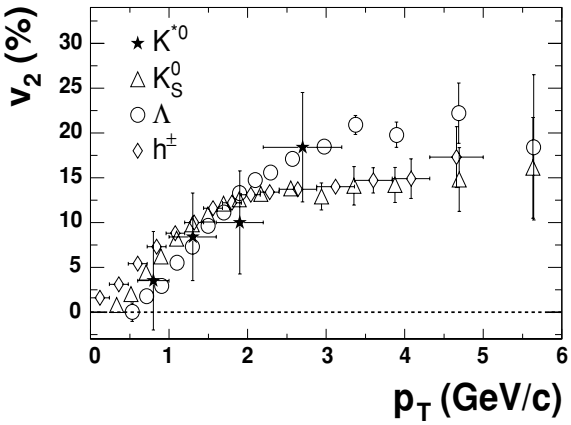

FIG. 15. The K^{*0} v_2 (filled stars) as a function of p_T for minimum bias Au+Au collisions compared to the K^0_S (open triangles), Λ (open circles), and charged hadron (open diamonds) v_2. The errors shown are statistical only.

$\langle\cos[2(\phi - \Psi_2)]\rangle$ is then calculated for each p_T bin. The finite resolution of the event plane angle, which is due to the limited number of tracks in the event plane calculation, reduces the measured K^{*0} v_2. Thus the obtained $\langle\cos[2(\phi - \Psi_2)]\rangle$ values are further corrected for an event plane resolution factor (<1) using the method presented in [57]. Figure 15 shows the K^{*0} v_2 as a function of p_T compared to the K^0_S, Λ, and charged hadron v_2 for minimum bias Au+Au collisions [27]. A significant nonzero K^{*0} v_2 is observed. Nevertheless, owing to the large uncertainties on the K^{*0} v_2 measurement, no significant difference is observed between the K^{*0} v_2 and the K^0_S, Λ, and charged hadron v_2.

To calculate the contributions to the K^* production from either direct quark or hadron combinations, the following function [58] was used to fit the K^{*0} v_2:

$$v_2(p_T, n) = \frac{an}{1 + \exp[-(p_T/n - b)/c]} - dn, \qquad (18)$$

where a, b, c, and d are constants extracted by fitting to the K^0_S and Λ v_2 data points in [58], and n is the open parameter standing for the number of constituent quarks. From the fit to the K^{*0} v_2, $n = 3 \pm 2$ was obtained. Because of the large statistical uncertainties, it is difficult to identify the K^* production fractions from direct quark combinations ($n = 2$) or hadron combinations ($n = 4$). About 15–20 times more Au+Au collision events were taken by the STAR experiment in the fourth RHIC run in 2004, which is expected to provide enough sensitivity for more precise calculations of n to identify the K^* from different production mechanisms.

F. Nuclear modification factor

The number of binary collisions (N_{bin}) scaled centrality ratio (R_{CP}) is a measure of the particle production dependence on the size and density of the collision system and is closely related to the nuclear modification factor (R_{AA}). Recent measurements of the Λ and K^0_S R_{CP} at RHIC [27] have shown that in the intermediate p_T region ($2 < p_T < 4$ GeV/c), the Λ and K^0_S R_{CP} are significantly smaller than unity. These

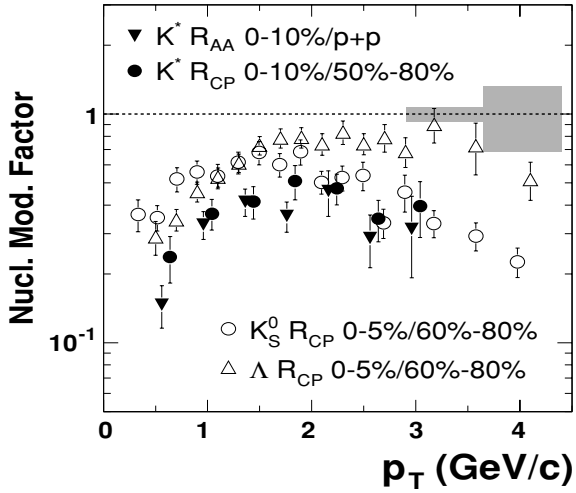

FIG. 16. The K^* R_{AA} (filled triangles) and R_{CP} (filled circles) as a function of p_T compared to the K^0_S (open circles) and Λ (open triangles) R_{CP}. The errors shown are statistical only. The dashed line represents the number of binary collisions scaling. The widths of the gray bands represent the systematic uncertainties of R_{AA} (left) and R_{CP} (right) resulting from the model calculations of N_{bin}.

measurements suggest that high-p_T jets lose energy through gluon radiation while traversing through dense matter. It has also been observed that the R_{CP} is significantly different for Λ and K^0_S with $p_T > 2$ GeV/c. It is not clear whether this R_{CP} difference is due to a mass or a particle species effect. The K^* is a meson but has a mass that is close to the Λ baryon mass. Thus, the measurement of the K^* R_{CP} may help in discriminating between mass or particle species effect at the intermediate-p_T region.

The K^* R_{CP} was obtained from the p_T spectra of the top 10% and the 50–80% most peripheral Au+Au collisions. The K^* R_{AA} was calculated from the p_T spectrum of the 10% most central Au+Au collisions and the p_T spectrum of the minimum bias $p + p$ collisions.

The K^* R_{AA} and R_{CP} as a function of p_T compared to the Λ and K^0_S R_{CP} are shown in Fig. 16. The K^* R_{AA} and R_{CP} for $p_T < 1.6$ GeV/c are smaller than the Λ and K^0_S R_{CP}, indicating the strong rescattering of the K^* daughters at low p_T. The rescattering of the K^* decay products is weaker for $p_T > 1.6$ GeV/c since K^* with larger p_T are more likely to decay outside the fireball [21]. Therefore, higher p_T K^* have a higher probability of being measured compared to low-p_T K^*. The K^* R_{AA} and R_{CP} are closer to the K^0_S R_{CP} and different from the Λ R_{CP} for $p_T > 1.6$ GeV/c. Thus, a strong mass dependence of the nuclear modification factor is not supported and a baryon-meson effect is favored in the particle production in the intermediate-p_T region.

VI. CONCLUSION

Results on the K^{*0} and $K^{*\pm}$ resonance production in Au+Au and $p + p$ collisions measured with the STAR experiment at $\sqrt{s_{NN}} = 200$ GeV were presented. The K^{*0}

and $K^{*\pm}$ signals were reconstructed via their hadronic decay channels $K^{*0} \to K\pi$ and $K^{*\pm} \to K^0_S\pi^\pm$ at midrapidity.

The K^{*0}/K yield ratios in Au+Au collisions were observed to be smaller than the ratio in $p+p$ interactions, which may be interpreted in the context of finite cross sections in a late hadronic phase. The result suggests that the rescattering of the K^{*0} decay products is dominant over the K^{*0} regeneration and therefore the reaction channel $K^* \leftrightarrow K\pi$ is not in balance. As a result, the K^{*0}/K^- yield ratio can be used to estimate the time between chemical and kinetic freeze-outs. Using the K^{*0}/K^- yield ratio, the lower limit of the time between chemical and kinetic freeze-outs is estimated to be at least 2 ± 1 fm/c.

A significant nonzero K^{*0} elliptic flow v_2 was measured as a function of p_T in minimum bias Au+Au collisions. Because of limited statistics, no conclusive statement can be made about the difference between the K^{*0} v_2 and the K^0_S, Λ, and charged hadron v_2. The estimated number of constituent quarks for the K^{*0} from the v_2 scaling according to Eq. (18) is 3 ± 2. Thus, improved statistics for Au+Au collision data are needed to identify the K^* production fractions from direct quark combinations or hadron combinations.

The K^{*0} nuclear modification factors R_{AA} and R_{CP} were measured as a function of p_T. Both the K^{*0} R_{AA} and R_{CP} are found to be closer to the K^0_S R_{CP} and different from the Λ R_{CP} for $p_T > 2$ GeV/c. A strong mass dependence of the nuclear modification factor is not observed. This establishes a baryon-meson effect over a mass effect in the particle production at the intermediate-p_T region.

ACKNOWLEDGMENTS

We thank the RHIC Operations Group and RCF at BNL and the NERSC Center at LBNL for their support. This work was supported in part by the HENP Divisions of the Office of Science of the U.S. DOE; the U.S. NSF; the BMBF of Germany; IN2P3, RA, RPL, and EMN of France; EPSRC of the United Kingdom; FAPESP of Brazil; the Russian Ministry of Science and Technology; the Ministry of Education and the NNSFC of China; Grant Agency of the Czech Republic, FOM and UU of the Netherlands, DAE, DST, and CSIR of the Government of India; Swiss NSF; and the Polish State Committee for Scientific Research.

[1] T. Blum, L. Karkkainen, D. Toussaint, and S. Gottlieb, Phys. Rev. D **51**, 5153 (1995).
[2] R. Rapp, Phys. Rev. C **66**, 017901 (2002).
[3] R. Rapp and E. V. Shuryak, Phys. Rev. Lett. **86**, 2980 (2001).
[4] C. Song and V. Koch, Phys. Rev. C **55**, 3026 (1997).
[5] J. Rafelski, J. Letessier, and G. Torrieri, Phys. Rev. C **64**, 054907 (2001).
[6] G. E. Brown and M. Rho, Phys. Rev. Lett. **66**, 2720 (1991).
[7] R. Rapp, Nucl. Phys. **A725**, 254 (2003).
[8] E. V. Shuryak and G. Brown, Nucl. Phys. **A717**, 322 (2003).
[9] J. Schaffner-Bielich, Phys. Rev. Lett. **84**, 3261 (2000).
[10] R. Rapp and J. Wambach, Adv. Nucl. Phys. **25**, 1 (2000).
[11] J. M. Link *et al*., Phys. Lett. **B535**, 43 (2002).
[12] J. Adams *et al*., Phys. Rev. Lett. **92**, 092301 (2004).
[13] M. Bleicher and H. Stöcker, J. Phys. G **30**, S111 (2004).
[14] R. S. Longacre, nucl-th/0303068.
[15] P. Braun-Munzinger (private communication).
[16] P. F. Kolb and M. Prakash, Phys. Rev. C **67**, 044902 (2003).
[17] W. Broniowski, W. Florkowski, and B. Hiller, Phys. Rev. C **68**, 034911 (2003).
[18] H. W. Barz *et al*., Phys. Lett. **B265**, 219 (1991).
[19] S. Pratt and W. Bauer, Phys. Rev. C **68**, 064905 (2003).
[20] P. Granet *et al*., Nucl. Phys. **B140**, 389 (1978).
[21] M. Bleicher *et al*., Phys. Lett. **B530**, 81 (2002).
[22] S. D. Protopopescu *et al*., Phys. Rev. D **7**, 1279 (1973).
[23] M. J. Matison *et al*., Phys. Rev. D **9**, 1872 (1974).
[24] M. Bleicher *et al*., J. Phys. G **25**, 1859 (1999).
[25] Z.-W. Lin and C. M. Ko, Phys. Rev. Lett. **89**, 202302 (2002).
[26] S. S. Adler *et al*., Phys. Rev. C **69**, 034909 (2004).
[27] J. Adams *et al*., Phys. Rev. Lett. **92**, 052302 (2004).
[28] C. Nonaka, B. Muller, M. Asakawa, S. A. Bass, and R. J. Fries, Phys. Rev. C **69**, 031902(R) (2004).
[29] C. Adler *et al*., Phys. Rev. Lett. **89**, 202301 (2002).
[30] M. Anderson *et al*., Nucl. Instrum. Methods A **499**, 659 (2003).
[31] C. Adler *et al*., Phys. Rev. Lett. **87**, 112303 (2001).
[32] K. Hagiwara *et al*., Phys. Rev. D **66**, 010001 (2002).
[33] C. Adler *et al*., Phys. Lett. **B595**, 143 (2004).
[34] C. Adler *et al*., Phys. Rev. Lett. **89**, 092301 (2002).
[35] C. Adler *et al*., Phys. Rev. C **66**, 061901(R) (2002).
[36] C. Adler *et al*., Phys. Rev. C **65**, 041901(R) (2002).
[37] J. Adams *et al*., Phys. Lett. **B612**, 181 (2005).
[38] K. Adcox *et al*., Phys. Rev. Lett. **89**, 092302 (2002).
[39] H. Zhang, Ph.D. thesis, Yale University, 2004.
[40] L. Gaudichet, Ph.D. thesis, SUBATECH, 2003.
[41] C. Adler *et al*., Phys. Rev. Lett. **89**, 272302 (2002).
[42] J. Adams *et al*., Phys. Rev. Lett. **92**, 112301 (2004).
[43] F. Becattini, Nucl. Phys. **A702**, 336 (2002).
[44] C. Adler *et al*., Phys. Rev. Lett. **87**, 112303 (2001).
[45] T. Sjostrand *et al*., Comput. Phys. Commun. **135**, 238 (2001).
[46] G. Wilk and Z. Wlodarczyk, Phys. Rev. Lett. **84**, 2770 (2000).
[47] E. Schnedermann, J. Sollfrank, and U. Heinz, Phys. Rev. C **48**, 2462 (1993).
[48] H. Albrecht *et al*., Z. Phys. C **61**, 1 (1994).
[49] M. Derrick *et al*., Phys. Lett. **B158**, 519 (1985).
[50] K. Abe *et al*., Phys. Rev. D **59**, 052001 (1999).
[51] Y. Pei, Z. Phys. C **72**, 39 (1996).
[52] J. Canter *et al*., Phys. Rev. D **20**, 1029 (1979).
[53] M. Aguilar-Benitez *et al*., Z. Phys. C **50**, 405 (1991).
[54] D. Drijard *et al*., Z. Phys. C **9**, 293 (1981).
[55] T. Akesson *et al*., Nucl. Phys. **B203**, 27 (1982).
[56] P. Braun-Munzinger *et. al*., Phys. Lett. **B518**, 41 (2001); J. Stachel (private communication).
[57] A. M. Poskanzer and S. A. Voloshin, Phys. Rev. C **58**, 1671 (1998).
[58] X. Dong *et al*., Phys. Lett. **B597**, 328 (2004).